

The effects of particle clustering on hindered settling in high-concentration particle suspensions

Yinuo Yao^{1,2,†}, Craig S. Criddle² and Oliver B. Fringer¹

¹The Bob and Norma Street Environmental Fluid Mechanics Laboratory, Department of Civil and Environmental Engineering, Stanford University, Stanford, CA 94305, USA

²Codiga Resource Recovery Center at Stanford, Department of Civil and Environmental Engineering, Stanford University, Stanford, CA 94305, USA

(Received 25 November 2020; revised 30 March 2021; accepted 10 May 2021)

We study the effects of Archimedes number Ar and volume fraction ϕ in three-dimensional, high concentration and monodispersed particle suspensions. Simulations were conducted using the immersed boundary method with direct forcing for triply periodic cases and with $Ar = 21\text{--}23\,600$ and $\phi = 0.22\text{--}0.43$. We find that cluster formation is strongly dependent on the Archimedes number but weakly dependent on the volume fraction for concentrated suspensions. Particles in low Ar cases are characterized by less frequent but long-lived clusters, resulting in higher hindered settling, while high Ar cases consist of more frequent but short-lived clusters, leading to reduced hindered settling. By quantifying the effects of collisions on the hydrodynamic fluctuations, we show that the lifespan of clusters for the low Ar cases is longer because particles are subject to appreciable wake interactions without collisions. On the other hand, clusters for high Ar cases are broken before being subject to appreciable wake interactions due to frequent collisions, leading to a shorter cluster lifespan. The results imply that there exists an Ar for particles in fluidized bed reactors that can reduce short circuiting due to clustering and enhance performance by maximizing flow–particle interactions. This result is consistent with existing reactor studies demonstrating that optimal particle diameters and Ar values correspond to cases with short-lived clusters, although more thorough experimental studies are needed.

Key words: fluidized beds, particle/fluid flow

1. Introduction

Sedimentation/suspension and fluidization are found in many natural and industrial systems such as wastewater treatment, chemical processes and sediment transport.

[†] Email address for correspondence: yaoyinuo@stanford.edu

In wastewater treatment, sedimentation is used to separate, through settling, both grit and organic particles (Burton *et al.* 2013; Scherson, Woo & Criddle 2014) and fluidized-bed reactors are widely used in treating both industrial and domestic wastewater (Shin *et al.* 2014; McCarty 2018; Shin & Bae 2018). More recently, fluidized particles have been used to reduce biological membrane fouling (Shin *et al.* 2016). In these applications, predicting the settling velocity in sedimentation or upflow velocity in fluidization provides valuable information for system design and operation.

Over the years, the general consensus has been to use a power-law model that relates the volume fraction ϕ to the velocity of interest \tilde{U} (settling velocity in sedimentation and upflow velocity in fluidization) (Richardson & Zaki 1954; Garside & Al-Dibouni 1977; Di Felice 1995; Yin & Koch 2007; Willen & Prosperetti 2019). The power law has been widely verified to be of the form

$$\frac{\tilde{U}}{w^*} = (1 - \phi)^n, \quad (1.1)$$

where \tilde{U} is the hindered settling velocity, w^* is the reference terminal velocity of a single particle in the domain of interest and n is the expansion index or power-law exponent (Richardson & Zaki 1954; Garside & Al-Dibouni 1977). In early studies, the main focus was to accurately model n as a function of the terminal Reynolds number in the domain of interest $Re_t^* = w^*d_p/\nu_f$, where d_p is the particle diameter and ν_f is the fluid kinematic viscosity. Defining U_t as the terminal velocity of a single particle in a finite-sized domain and $U_{t,\infty}$ as that in an infinitely large domain, a stepwise relationship between n and $Re_{t,\infty} = U_{t,\infty}d_p/\nu_f$ was proposed by Richardson & Zaki (1954) by using experimental data with concentrated volume fraction ($\phi > 0.05$) as

$$n = \begin{cases} 4.65, & Re_{t,\infty} < 0.2, \\ 4.35Re_{t,\infty}^{-0.03}, & 0.2 \leq Re_{t,\infty} < 1, \\ 4.45Re_{t,\infty}^{-0.1}, & 1 \leq Re_{t,\infty} < 500, \\ 2.39, & Re_{t,\infty} \geq 500. \end{cases} \quad (1.2)$$

Garside & Al-Dibouni (1977) improved the relationship with a continuous sigmoid function proposed to relate the expansion exponent n to $Re_t = U_td_p/\nu_f$ as

$$n = \frac{5.1 + 0.27Re_t^{0.9}}{1 + 0.1Re_t^{0.9}}, \quad (1.3)$$

which was found to improve the accuracy of the power law by 20 %–30 % (Yin & Koch 2007). As Re_t and $Re_{t,\infty} \rightarrow 0$, $n \rightarrow 4.65$ in (1.2) and 5.1 in (1.3).

Batchelor (1972), on the other hand, predicted the theoretical hindered settling velocity of monodispersed particles for a dilute suspension in viscous flow and showed that n would be 6.5 for small Péclet number and 5.5 for large Péclet number suspensions (Batchelor & Wen 1982), where the Péclet number is a ratio of the relative effects of gravity to Brownian diffusion. Di Felice (1999) discovered that n is the same in both dilute and concentrated suspension in the viscous regime ($Re_t \ll 1$) which is supported by computing n in the limit of large Péclet number in (1.3). However, n becomes approximately 1.5 times smaller in concentrated suspensions for intermediate terminal Reynolds numbers, leading to a lower hindered settling velocity in concentrated suspensions. This indicates a deceleration as the volume fraction transitions from dilute to concentrated suspensions. If there was no

deceleration in the concentrated regime, n would be the same for both regimes over all Reynolds numbers. To address this discrepancy in the hindered settling velocity, many researchers (Di Felice 1995, 1999; Yin & Koch 2007; Hamid, Molina & Yamamoto 2014; Zaidi, Tsuji & Tanaka 2015; Willen & Prosperetti 2019) proposed to include a prefactor k that typically ranges from 0.8 to 0.9 and proposed the modified power law

$$\frac{\tilde{U}}{w^*} = k(1 - \phi)^n. \quad (1.4)$$

In addition, as Re_t increases, the prefactor k for the power-law model that is satisfied for both the dilute and concentrated suspensions also decreases (Yin & Koch 2007). Some studies also suggest k in the range 0.8–0.9 for concentrated suspensions ($\phi > 0.05$) (Chong, Ratkowsky & Epstein 1979; Di Felice 1995). Di Felice (1995) conjectured that this discrepancy might be correlated to the size of particles.

Many studies have shown that particles tend to form clusters in dilute suspensions (Li *et al.* 1991; Uhlmann & Doychev 2014; Capecelatro, Desjardins & Fox 2015; Fullmer & Hrenya 2017). The first mechanism is cluster-induced turbulence (known as CIT) which occurs when the system has a mass loading $\psi \gg 1$, where ψ is defined as

$$\psi = s \frac{\phi}{1 - \phi}, \quad (1.5)$$

where $s = \rho_p / \rho_f$ is the particle to fluid density ratio and ρ_p and ρ_f are the respective particle and fluid densities. In most experiments conducted to correlate n and k to Re_t (Richardson & Zaki 1954; Garside & Al-Dibouni 1977; Yin & Koch 2007; Willen & Prosperetti 2019), $s \sim O(0.1-1)$, and hence cluster-induced turbulence is unlikely to occur. Another cluster formation mechanism is wake interaction. Wake interactions are observed when the Archimedes number Ar or Galilei number Ga exceed some threshold (Uhlmann & Doychev 2014) where Ar and Ga are defined as

$$Ar = Ga^2 = \frac{g(s - 1)d_p^3}{\nu_f^2}, \quad (1.6)$$

where g is the gravitational acceleration. Most of the studies on particle clustering focus on dilute instead of concentrated suspensions. To date, no explanations have been provided to address the deviation of k from unity in concentrated suspensions. Therefore, a better understanding of the mechanisms governing and affecting k is required. For the remainder of this paper, the reference velocity in (1.1) and (1.4) will be denoted as U_t , the settling velocity of a single particle in the domain of interest, since the simulations are conducted in periodic domains without wall effects.

While sedimentation and fluidization can be studied with experiments or simulations, the advantage of experiments is the ability to test a large number of different particle parameters which is beneficial for establishing a relationship between Re_t and n . However, the main disadvantage of experiments is the difficulty in tracking individual particle information over time, leading to challenges in understanding both the fluid microstructure and microscopic particle behaviour. High-fidelity particle resolved simulations (PRS) simulate the movement of particles over time by resolving the flow around each particle, enabling accurate quantification of fluid–particle interactions. Therefore, tracking information of individual particles over time is possible, which enables the examination of microstructure and improves understanding of the mechanisms governing particle motion.

To understand the dependence of the prefactor k on different non-dimensional parameters, a formal dimensional analysis is conducted. We consider a case when a cloud of particles is settling or fluidized with volume fraction ϕ in a periodic domain of horizontal extent L . The hindered/superficial velocity is related to six dimensional parameters and the non-dimensional volume fraction ϕ with

$$\tilde{U} = f(d_p, v_f, \rho_f, \rho_p, g, L, \phi). \quad (1.7)$$

Dimensional analysis results in a total of four dimensionless groups. Choosing ρ_p, v_f and d_p to non-dimensionalize the other parameters results in the functional relationship

$$Re_p = f(\phi, Ar, s, d_p/L), \quad (1.8)$$

where the particle Reynolds number is defined as

$$Re_p = \frac{\tilde{U} d_p}{v_f}. \quad (1.9)$$

For the range of density ratios of interest, we will show that the results weakly depend on s . Furthermore, in a sufficiently large periodic domain, the dependence on d_p/L vanishes. Therefore, the only parameters governing the particle Reynolds number are ϕ and Ar , implying

$$Re_p = f(\phi, Ar). \quad (1.10)$$

Therefore, we expect any non-dimensional parameter, including the prefactor k in (1.4), to depend on just two non-dimensional parameters. Since the literature suggests that the term $(1 - \phi)^n$ in (1.4) largely captures the effects of ϕ , we can further assume that k depends primarily on one parameter, namely Ar .

In this paper, we use PRS of monodispersed particle suspensions to understand the effects of the Archimedes number and particle density ratio on the hindered settling velocity. A series of simulations are analysed to understand the relationship between Ar and the prefactor k in (1.4), and we explain the results in the context of detailed fluid-particle physics.

2. Numerical methodology and simulation set-up

2.1. Equations and discretizations

The governing Navier–Stokes equations are solved in a three-dimensional cubic domain containing an array of uniform spherical particles. To enforce no-slip boundary conditions on the particle surfaces, a source term, \mathbf{f}_{IBM} , based on the direct-forcing immersed boundary method (IBM) method is added to the incompressible Navier–Stokes equation to give

$$\frac{\partial \mathbf{u}}{\partial t} + \mathbf{u} \cdot \nabla \mathbf{u} = -\nabla p + \nu_f \nabla^2 \mathbf{u} + \mathbf{f}_{IBM}, \quad (2.1)$$

subject to continuity, $\nabla \cdot \mathbf{u} = 0$, where \mathbf{u} is the velocity vector and p is the pressure normalized by the fluid density, ρ_f . These equations are discretized on a uniform collocated Cartesian grid. A fractional step method (Zang, Street & Koseff 1994) is used to couple the momentum and pressure. The advection term is discretized with the explicit, three-step Runge–Kutta scheme described in Rai & Moin (1991). The viscous term is discretized with the implicit Crank–Nicolson scheme to eliminate the associated stability constraint. The linear systems arising from the implicit discretization of the viscous terms and the

pressure Poisson equation are solved using the HYPRE library (Chow, Cleary & Falgout 1998; Falgout & Yang 2002). To solve the interactions between the fluid and the particles, the direct forcing approach first proposed by Uhlmann (2005) and improved by Kempe & Fröhlich (2012b) is adopted. Since the IBM formulation is unable to resolve the fluid–particle interactions when the particles are less than two grid cells apart, we follow the approach by Biegert, Vowinkel & Meiburg (2017) who employ the collision model proposed by Kempe & Fröhlich (2012a).

2.2. Numerical method validation

To test the methodology, we simulated a single particle settling in a three-dimensional domain with a quiescent fluid under the influence of gravity and compared the results with published values. Simulated particle settling is compared with the experimental result of ten Cate *et al.* (2002) (figure 1a) in which a particle settles in the negative z -direction onto a bottom, no-slip wall, with $Re_t = 12$. Particle settling is also compared with the results of Mordant & Pinton (2000) (figure 1b), in which a particle is allowed to come to terminal velocity with $Re_t = 360$. The domain sizes are $6.66d_p \times 6.66d_p \times 13.33d_p$ for the wall-bounded case and $7.5d_p \times 7.5d_p \times 60d_p$ for the terminal settling case. The boundary conditions are periodic in all directions for the terminal settling case and periodic in the x - and y -directions with no-slip top and bottom walls for the wall-bounded cases. In all cases, a particle is initialized in the horizontal centre and $2d_p$ from the top of the domain with no vertical velocity in a quiescent fluid. The kinematic viscosity is $\nu_f = 1.175 \times 10^{-4} \text{ m s}^{-2}$ for the wall-bounded case and $\nu_f = 5.416 \times 10^{-3} \text{ m s}^{-2}$ for the terminal settling case, and the fluid and particle densities are $\rho_f = 1000$ and $\rho_p = 1164 \text{ kg m}^{-3}$ (figure 1a) and $\rho_f = 1000$ and $\rho_p = 2560 \text{ kg m}^{-3}$ (figure 1b). The time-step size is dictated by requiring a maximum Courant number of $U_t \Delta t / h = 0.5$, where $h = \Delta x = \Delta y = \Delta z$ is the grid spacing which is uniform in the x -, y - and z -directions. We perform simulations with different resolutions to determine the resolution needed to reproduce the published results. As shown in figure 1, for the wall-bounded case (figure 1a), the particle approaches its terminal settling velocity but then decelerates upon reaching the wall, while in figure 1(b) the particle reaches its terminal velocity. In both cases, the settling velocity is normalized by the reference velocity $w_{t,ref} = \sqrt{gd_p}$ and the time is normalized by the reference time $t_{t,ref} = \sqrt{d_p/g}$. The results indicate that our simulations agree with published results when $d_p/h = 20$ – 30 grid points are used to resolve the flow around the particles, which is consistent with previous PRS simulations (Uhlmann 2005; Kempe & Fröhlich 2012b; Biegert *et al.* 2017).

To validate the collision model, the simulation results were compared with the experiments of Gondret, Lance & Petit (2002), in which a particle bounces off the wall of a tank. The experiments focus on the effect of the Stokes number on the maximum height of the particle after bouncing, where the Stokes number is defined as

$$St_{val} = \frac{\rho_p d_p u_{in}}{9 \rho_f \nu_f}, \quad (2.2)$$

where u_{in} is the impact velocity. The parameters used in the simulations were identical to Biegert *et al.* (2017), and we simulate $St_{val} = 27$ (figure 2a) and $St_{val} = 152$ (figure 2b). The domain sizes in these simulations are $13.33d_p \times 13.33d_p \times 26.66d_p$ for figure 2(a) and $6.67d_p \times 6.67d_p \times 66.7d_p$ for figure 2(b), and $d_p/h = 19.2$ grid points are used to resolve the particle diameter. The boundary conditions on the sidewalls are periodic with no-slip conditions on the top and bottom boundaries. Simulations are initialized with the

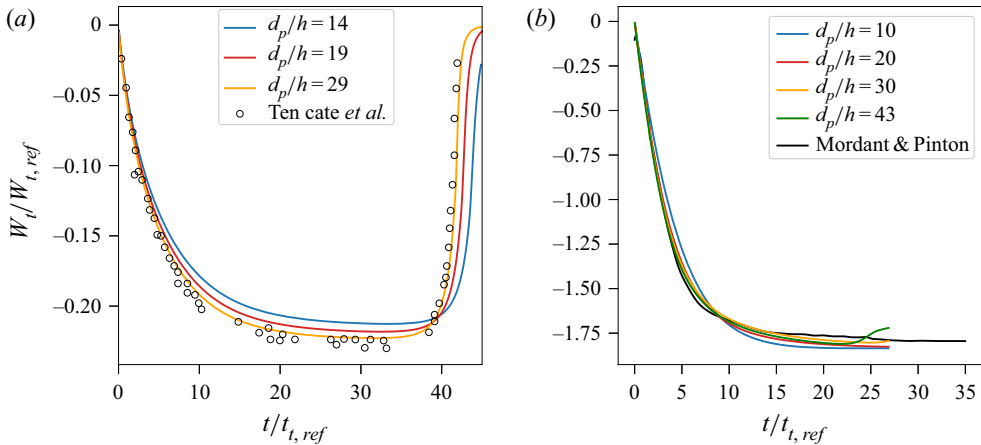


Figure 1. Time series of the simulated settling velocity U_t of a single particle with (a) $Re_t = 12$ and (b) $Re_t = 360$ and different grid resolutions h used to resolve the particle diameter d_p , compared with published results.

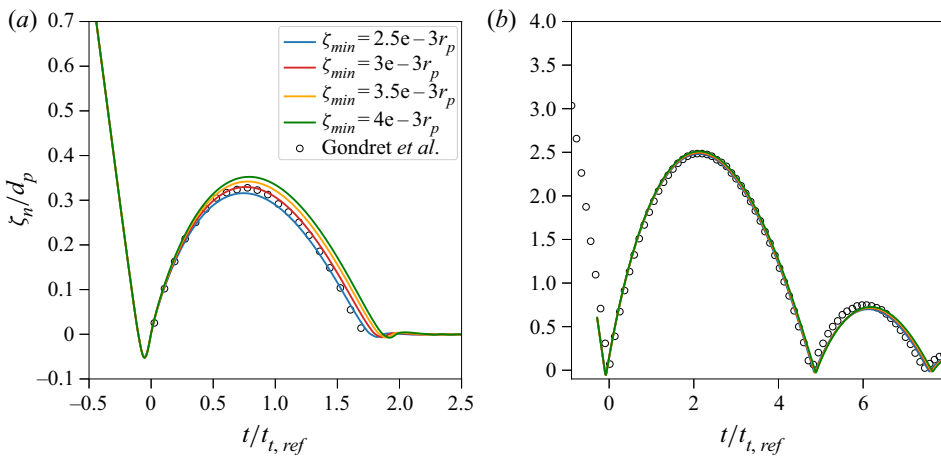


Figure 2. Simulated height of the centre of a particle (ζ_n) bouncing off of a wall with (a) $St_{val} = 27$ and (b) $St_{val} = 152$ compared with published values. The minimum distance from the wall is ζ_{min} .

particle at rest in a quiescent fluid with kinematic viscosity $\nu_f = 1.036 \times 10^{-4} \text{ m s}^{-2}$ for figure 2(a) and $\nu_f = 1.070 \times 10^{-5} \text{ m s}^{-2}$ for figure 2(b) and density ratio $s = 8.083$ for figure 2(a) and $s = 8.342$ for figure 2(b). Before reaching a distance $\zeta_n = d_p/2$ from the wall, the particle velocity is prescribed as the velocity in the z -direction

$$u(t) = -u_{in}(1 - e^{-40t}). \quad (2.3)$$

The prescribed particle velocity is then removed when $\zeta_n < d_p/2$, whereupon the particle is subject to velocity interactions with the fluid and wall. To account for lubrication effects, the collision model proposed by Biegert *et al.* (2017) requires a parameter dictating the minimum spacing between the particle and wall, setting the maximum lubrication force. Figure 2 shows the effect of different minimum spacing parameters and demonstrates that our results match the experiments when $\zeta_{min} = 2.5 \times 10^{-3} r_p$,

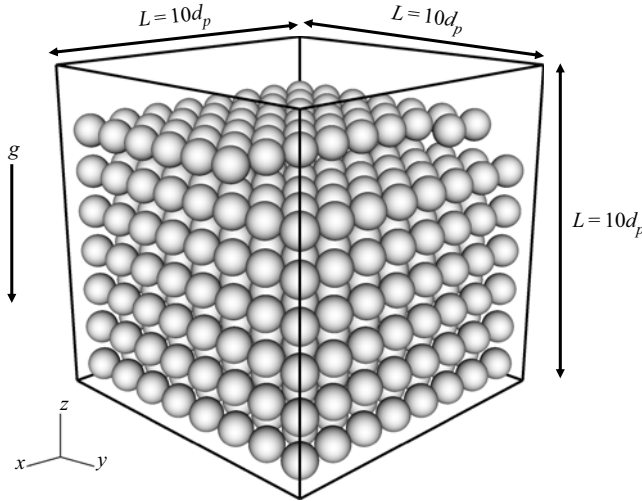


Figure 3. Initial particle positions in the periodic simulation domain with $N_p = 817$ particles and a volume fraction $\phi = 0.43$.

where r_p is the particle radius. We use this minimum distance in the collision model for all simulations in this paper.

2.3. Simulation set-up for particle clustering

Three-dimensional simulations are conducted in a cubic, triply periodic domain, as shown in figure 3. The particles have a uniform diameter $d_p = 2$ mm and density ρ_p that is varied to give different values of s , and the fluid has a density $\rho_f = 998.21$ kg m⁻³. The grid spacing is uniform in all directions and given by $\Delta x = \Delta y = \Delta z = h = d_p/25.6$, which is sufficient to resolve the flow–particle interactions as demonstrated in § 2.2. The cubic domain has a side length $L = 10d_p$, giving a three-dimensional grid with $256 \times 256 \times 256$ grid points. Yin & Koch (2007) showed that accurate PRS of particle suspensions with low Re_t can be achieved with a cubic domain with $L \approx 10d_p$ by applying a correction based on the structural factor (see § 3.3). The time step is determined based on the advection and diffusion Courant number which are defined as $C_{adv} = \tilde{U}\Delta t/h$ and $C_{diff} = \nu_f \Delta t/h^2$, respectively, resulting in a maximum Courant number $C_{max} = \max(C_{adv}, C_{diff}) = 0.25$.

Based on the dimensional analysis, the prefactor k is primarily a function of Ar , hence the parameter of interest is Ar as defined in (1.6). To fit n and k using (1.4), simulations were conducted with three volume fractions $\phi = 0.22, 0.30, 0.43$, five Archimedes numbers $Ar = 21, 100, 1000, 7413, 23\,600$ and three density ratios $s = 1.3, 2.46, 6$. To obtain the desired volume fraction ϕ , we compute the number of particles N_p with fixed L and d_p .

The desired values of Ar are achieved by varying the ratio of $(s - 1)/\nu_f^2$ such that $N_p = 434, 581, 817$ for $\phi = 0.22, 0.30, 0.43$. A total of 33 simulations were conducted as shown in table 1. All simulations are initialized with particles equally spaced in the domain (see figure 3) and the flow is initialized as static in all directions. The gravitational force leads to the settling and random motion of the particles until statistical equilibrium is reached, at which time the dynamics are independent of the initial particle distribution.

Defining the ensemble average over all particles with $\langle \{\cdot\} \rangle$, figure 4 shows that the magnitude of the instantaneous ensemble settling velocity $\langle U_z \rangle$ initially increases with

	$Ar = 21$	$Ar = 100$	$Ar = 1000$	$Ar = 7413$	$Ar = 23\,600$
s	1.30, 2.46, 6.00	1.30	1.30	1.30, 2.46, 6.00	1.30, 2.46, 6.00
N_p			434, 581, 817		
ϕ			0.22, 0.30, 0.43		
Cases varying s and ϕ	9	3	3	9	9
Total no. of cases			33		

Table 1. Summary of parameters used in the simulations. Each column represents parameters with different s while varying $v_f = [g(s-1)d_p^3/Ar]^{1/2}$ to ensure the desired Ar . Simulations with each Ar and s were conducted three times with different ϕ by varying N_p . The particle diameter and fluid density are held fixed at $d_p = 0.002$ m and $\rho_f = 998.21$ kg m⁻³, and the domain size is fixed at $L = 10 d_p$.

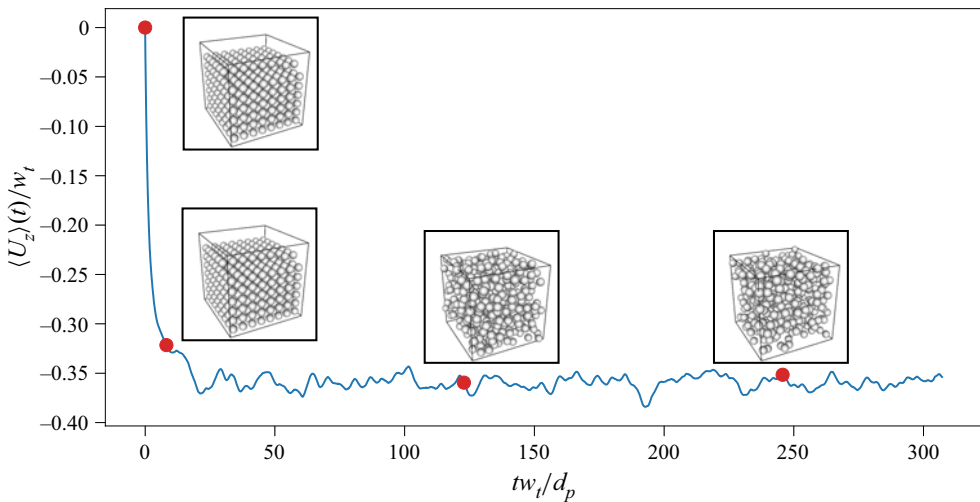


Figure 4. Time series of the ensemble settling velocity $\langle U_z \rangle$ normalized by U_t for $Ar = 7413$, $s = 1.3$ and $\phi = 0.43$.

time as particles rearrange and settle. It eventually reaches statistical equilibrium once the average drag force in the vertical balances the weight of the particles. We compute the settling velocity of a single particle in an infinitely large domain, U_t that satisfies the expression (Yin & Koch 2007)

$$Ar = \begin{cases} 18Re_t \left[1 + 0.1315Re_t^{(0.82-0.05 \log_{10} Re_t)} \right], & 0.01 < Re_t < 20, \\ 18Re_t \left[1 + 0.1935Re_t^{0.6305} \right], & 20 < Re_t < 260. \end{cases} \quad (2.4)$$

Various researchers have shown that equation (2.4) has an error ranging from 2 % to 4 % when compared with simulations of single particle settling in a periodic domain with d_p/L ranging from 0.1 to 0.05. Yin & Koch (2007) have shown that as the size of domain L increases and d_p/L decreases, U_t converges to the value calculated with (2.4). Therefore, $d_p/L = 0.1$ is sufficient to obtain results with error less than 4 %. Simulations are run for $t_{max} = 200\text{--}500\tau_T$ to obtain statistically converged results, where $\tau_T = d_p/U_t$ is defined as the particle turnover time. Time-average statistics are denoted by the overbar and computed

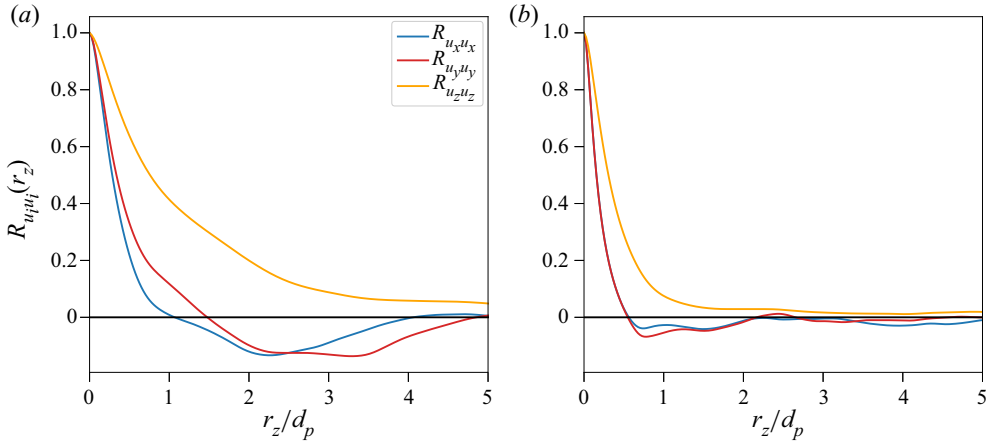


Figure 5. Two-point autocorrelation of Eulerian velocity fluctuations as a function of r_z for $Ar =$ (a) 21 and (b) 23 600.

over $50\tau_T$ such that

$$\overline{\{\cdot\}} = \frac{1}{50\tau_T} \int_{t_i}^{t_{max}} \{\cdot\} dt, \quad (2.5)$$

where $t_i = t_{max} - 50\tau_T$. Using these definitions, the time-averaged ensemble settling velocity is given by $\langle \overline{U_z} \rangle$, which we refer to as the hindered settling velocity \tilde{U} in what follows.

2.4. Evaluation of domain size

To evaluate the appropriateness of the domain size, we compute the two-point autocorrelation of Eulerian velocity fluctuations as

$$R_{u_i u_i}(r_j) = \frac{\langle u'_i(x_{0,j}) u'_i(x_{0,j} + r_j) \rangle}{\langle u'_i(x_{0,j}) u'_i(x_{0,j}) \rangle}, \quad (2.6)$$

where $x_{0,j}$ is a reference point in the domain, i and $j = x, y, z$ and $u'_i = u_i - \langle u_i \rangle$ is the Eulerian velocity fluctuation and $\langle u_i \rangle$ is the Eulerian spatially averaged velocity in all directions. Due to periodicity in all directions, we compute the two-point autocorrelation for half of the domain. Figure 5 shows the two-point autocorrelation as a function of z $R_{u_i u_i}(r_z)$ for cases with $Ar = 21$ and 23 600. Overall, due to the presence of a mean flow in the z -direction, the decorrelation lengths are larger for fluctuations in u_z than for u_x and u_y . As Ar increases, the decorrelation length decreases because the velocity fluctuations are more restricted to be local. For $Ar = 21$ in the Stokes regime, $R_{u_z u_z}(r_z)$ decreases and converges to approximately 0.05, indicating nearly complete decorrelation. A similar trend is observed in the simulation by Uhlmann & Doychev (2014) with dilute suspensions of larger Ar particles. The authors conclude that a further increase in domain size would not fully decorrelate the Eulerian velocity fluctuations. For the case of $Ar = 23\,600$, the decorrelation lengths are approximately 2 and $3d_p$ for the respective transverse (x - and y -directions) and axial directions. With this analysis, we conclude that the domain size in this study is sufficient for complete decorrelation for high Ar cases and nearly complete for low Ar cases. For low Ar cases, given the current trend where the slope of the two-point autocorrelation function is approximately zero, a further increase in domain size is unlikely

to completely decorrelate the Eulerian velocity fluctuations. Nevertheless, the largest magnitude of the two-point autocorrelation $R_{u_z u_z}(r_z)$ is no bigger than approximately 0.05 for the case with the smallest value of Ar in this study.

3. Results and discussion

3.1. Power-law behaviour and effect of Archimedes number on k

For the cases with $Ar = 21$, $Re_t \approx 1$ results in Stokes law behaviour in which the finite periodic domain affects hindered settling velocity \tilde{U} . To correct the error associated with the finite domain size associated with Stokes flow, Yin & Koch (2007) used a correction method that relates the unbounded mean hindered settling velocity to the domain size with

$$\tilde{U} = \begin{cases} \langle \overline{U_z} \rangle + 1.7601 S_0 \frac{|F|}{3\pi d_p \rho_f \nu_f^*} \left(\frac{\pi}{6}\right)^{1/3} \left(\frac{d_p}{L}\right), & Ar \leq 21, \\ \langle \overline{U_z} \rangle, & Ar > 21, \end{cases} \quad (3.1)$$

where $\langle \overline{U_z} \rangle$ is the hindered settling velocity in the bounded domain, S_0 is the structure factor in an unbounded suspension in the limit of zero wavenumber, $F = (\rho_p - \rho_f)\pi d_p^3 g/6$ is the buoyancy force of a single particle and ν_f^* is the apparent dynamic viscosity that can be approximated as (Ladd 1989)

$$\nu_f^* = \nu_f(1 + 2.5\phi + 5\phi^2). \quad (3.2)$$

Here, S_0 is estimated using the Carnahan–Stirling approximation as

$$S_0 = \frac{(1 - \phi)^4}{1 + 4\phi + 4\phi^2 - 4\phi^3 + \phi^4} \quad (3.3)$$

which is applicable for $\phi > 0.05$ (Yin & Koch 2007).

Table 2 and figure 6 show the least squares fit of the normalized average hindered settling velocity $U^* = \langle \overline{U_z} \rangle / U_t$ to the power law given by (1.4). Also shown are results of fluidization in a doubly periodic domain with $N_p = 2000$ particles and $Ar = 23\,600$ but with six values of ϕ (details in the Appendix). Since the regression of these results overlaps those in this paper, we are confident that three values of ϕ is sufficient to regress for k . In addition, each regression gives n and k values that fit equation (1.4) with coefficients of determination $R^2 = 1.0$. The fitted values of n are consistent with the predictions from (1.2) and (1.3). Since the effects of the density ratio s on n and k are negligible, from now on we report on results with $s = 1.3$ and ignore results with $s = 2.46$ and 6.0 .

When plotted as a function of Ar as in figure 7, the magnitude of k decreases as Ar increases, indicating overprediction of \tilde{U} with the original power-law equation (1.1). Therefore, a prefactor $k < 1$ is needed to correct this overprediction. This result agrees with Di Felice & Parodi (1996) and Chong *et al.* (1979) that the prefactor k should be included even for concentrated particle suspensions and also suggests that the mechanism leading to the overprediction is stronger for higher values of Ar . An exponential function of the form of $k = k_0 \exp(-\alpha Ar)$, where k_0 and α are fitted parameters, is used to fit the data shown in figure 7. After regression, the relationship between k and Ar fits the relation

$$k = 0.89 \exp\left(-\frac{Ar}{10^5}\right), \quad (3.4)$$

with a coefficient of determination $R^2 = 0.86$. As $Ar \rightarrow 0$, $k \rightarrow 0.89$. We note that (3.4) is only valid for the range of Ar that we study ($21 \leq Ar \leq 2360$) and, while it

Ar	s	n	k	n_{rz}	n_{ga}
21	1.30	4.63 ± 0.08	$0.88 \pm \exp(0.03)$	4.44	4.87
21	2.46	4.60 ± 0.02	$0.88 \pm \exp(0.08)$	4.44	4.87
21	6.00	4.62 ± 0.01	$0.89 \pm \exp(0.005)$	4.44	4.87
100	1.30	4.31 ± 0.01	$0.87 \pm \exp(0.003)$	3.87	4.48
1000	1.30	3.46 ± 0.06	$0.81 \pm \exp(0.02)$	3.25	3.59
7413	1.30	3.01 ± 0.05	$0.78 \pm \exp(0.02)$	2.83	3.04
7413	2.46	3.02 ± 0.08	$0.79 \pm \exp(0.03)$	2.83	3.04
7413	6.00	3.04 ± 0.05	$0.80 \pm \exp(0.03)$	2.83	3.04
23 600	1.30	2.80 ± 0.05	$0.72 \pm \exp(0.02)$	2.39	2.73
23 600	2.46	2.77 ± 0.04	$0.72 \pm \exp(0.02)$	2.39	2.73
23 600	6.00	2.78 ± 0.02	$0.73 \pm \exp(0.01)$	2.39	2.73

Table 2. Fitted expansion exponent, n , and prefactor, k , along with 95 % confidence intervals that provide the best fits to equation (1.4). All fits have $R^2 = 1.0$.

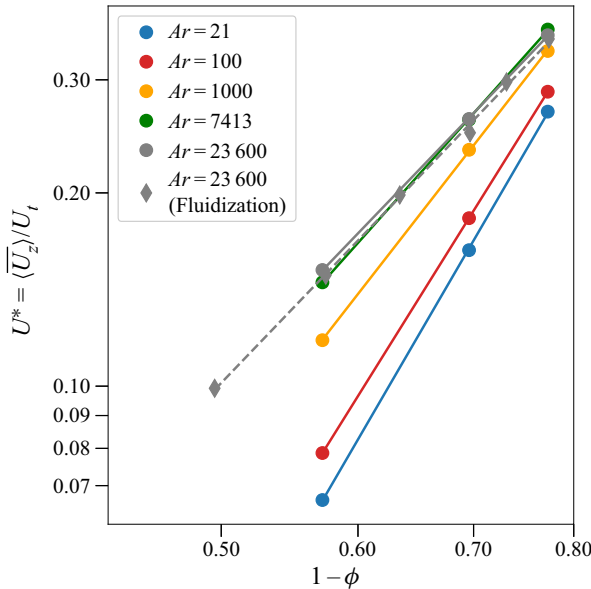


Figure 6. Normalized hindered settling velocity u^* as a function of porosity $1 - \phi$ for different Archimedes numbers Ar . Since the effect of the density ratio $s = \rho_p / \rho_f$ is negligible, we only show results for $s = 1.3$. The dashed line is a regression based on six values of ϕ from simulations described in the Appendix.

reproduces the $Ar \rightarrow 0$ limit, it should not be used to interpret the $Ar \rightarrow \infty$ limit. According to Di Felice (1999), the relationship between hindered settling and the volume fraction can be accounted for by two sets of parameters for dilute and concentrated suspension, respectively. Comparing with concentrated suspensions, n is higher to account for acceleration (Batchelor 1972, 1988) and $k = 1$ is used to recover U_t as $\phi \rightarrow 0$ in dilute suspensions. In our work, since (1.4) fits with $\phi > 0.05$, $k \neq 1$ and decreases as Ar decreases to account for lower hindered settling. This result agrees with various researchers (Di Felice & Parodi 1996; Yin & Koch 2007; Willen & Prosperetti 2019). As $Ar \rightarrow \infty$ (turbulent regime), the effects of Ar and ϕ on n and k are less well studied. Kowe *et al.*

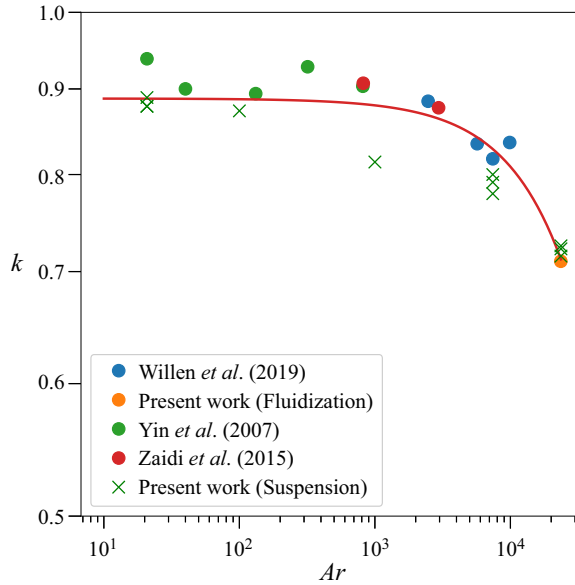


Figure 7. Prefactor k as a function of Ar from various publications and the present work along with the best-fit curve given by (3.4).

(1988) suggests that $n \rightarrow 1.5$ as $Ar \rightarrow \infty$, although more work is required to understand the effects on k .

3.2. Particle velocity fluctuations

We hypothesize that the lower hindered settling velocity at high Ar indicated by smaller k is due to weaker particle clustering effects. Uhlmann & Doychev (2014) demonstrated the important effects of long-lived clusters for higher hindered settling velocity u at moderate Ar with low ϕ . In our simulations, clusters persist for longer periods for lower Ar , implying that clustering will likely have more of an impact for low Ar cases. On the other hand, particles collide more often and clusters are easily broken for higher Ar , implying that collisions will likely have more of an impact for high Ar .

To understand the details of the particle motions, we computed the variance of the vertical velocity fluctuation as

$$\overline{\langle U_z^2 \rangle} = \overline{\langle (U_{z,n} - \langle U_z \rangle)^2 \rangle}, \quad (3.5)$$

where $U_{z,n}$ is the vertical velocity of particle $n = 1, \dots, N_p$. Figure 8 shows the variance of the vertical velocity fluctuations normalized by the square of the hindered settling velocity $\overline{\langle U_z \rangle}^2$ as a function of Ar for different ϕ . In general, as Ar increases, the normalized velocity fluctuation variance decreases possibly due to decreased wake interactions between particles at higher Ar . At high Ar , the effects of collisions (see § 3.5) dominate over the hydrodynamic forces, hence reducing the effect of wake interactions and normalized vertical velocity fluctuation variance. Interestingly, the lowest velocity fluctuation variance occurs when $\phi = 0.43$ and $Ar = 21$, while this value of ϕ produces the largest variance when $Ar > 1000$.

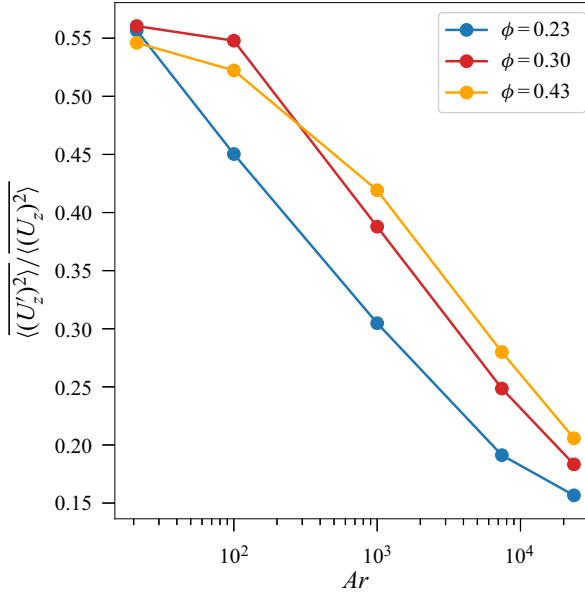


Figure 8. Normalized vertical velocity fluctuation variance $\overline{\langle (U'_z)^2 \rangle} / \overline{\langle (U_z)^2 \rangle}$ as a function of Ar for different ϕ .

3.3. Frequency spectrum of particle velocity fluctuations

As discussed in § 3.2, the largest normalized vertical velocity fluctuation variance is observed at the lowest value of $Ar = 21$. Uhlmann & Doychev (2014) discovered that clustering results in significant velocity fluctuations in dilute suspensions. Here, we compute the normalized ensemble-averaged frequency spectrum $\bar{E}(f) = E(f)/w_{ref}^2$ as the square of Fourier coefficients of the particle vertical velocity fluctuations as a function of the normalized frequency $\hat{f} = fd_p/w_{ref}$, where the reference velocity w_{ref} is defined as

$$w_{ref} = \sqrt{(s-1)gd_p}. \quad (3.6)$$

Figure 9 shows the normalized frequency spectra with different Ar for $\phi = 0.23$. Similar trends are observed for $\phi = 0.30$ and 0.43 (not shown). We also include the simulation of a fluidized bed with $Ar = 23\,600$ to demonstrate the independence of domain size. Details of this set-up can be found in the Appendix. The trends of these two cases with $Ar = 23\,600$ are almost identical except for the magnitude of the spectra even though the length of the fluidized bed (solid black line) is five times higher than the length of the domain in this paper, hence indicating that the spectra are weakly dependent on the domain size.

The spectra for all values of Ar are approximately constant at low frequencies. The range of frequencies for constant spectra is proportional to Ar while the magnitude of the constant spectra is inversely proportional to Ar . Both observations are likely due to the dependence of the terminal velocity U_t on Ar . The magnitude of particle velocity fluctuations increases with increasing Ar resulting in greater constant spectrum magnitudes. As the terminal velocity increases with increasing Ar , the normalized domain frequency $\hat{f}_{res} = U_t d_p / L w_{ref}$ also increases, resulting in a wider frequency range for constant spectra. Eventually, the spectra decrease and diverge from one another when $\hat{f}_t \geq \hat{f}_{res}$ following an approximate $-10/3$ slope for all Ar cases, indicating a power-law relation between the spectra and frequencies.

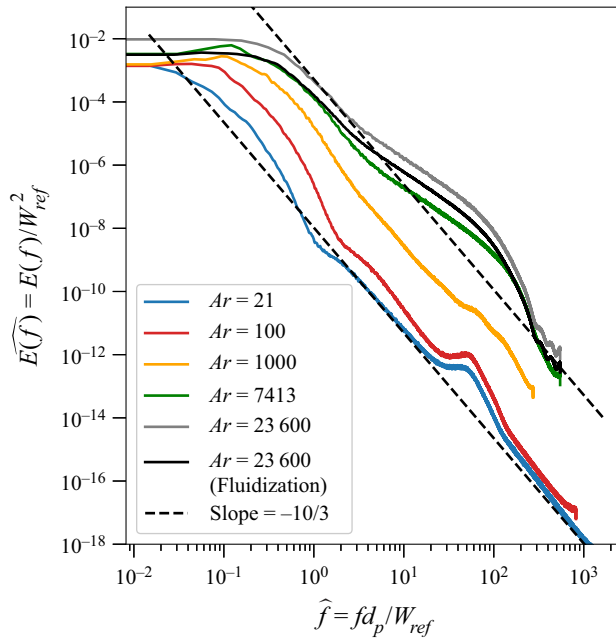


Figure 9. Normalized frequency spectra $\widehat{E}(f)$ as a function of normalized vertical particle velocity fluctuation frequency \widehat{f} for different Ar and $\phi = 0.23$.

Spectral slopes have been discussed in the context of Eulerian velocity fluctuations in bubbly flows, for which slopes ranging from $-8/3$ to -3 have been found (Lance & Bataille 1991; Rensen, Luther & Lohse 2005; Riboux, Risso & Legendre 2010; Lai & Socolofsky 2019; Bordoloi *et al.* 2020), and in gas–solid fluidized beds, for which the spectral slopes of pressure fluctuations range from -4 to -2 (Johnsson *et al.* 2000; van Ommen *et al.* 2011; van der Schaaf *et al.* 2002). While the slope of $-10/3$ in our simulations is in the range of spectral slopes in the literature, at this time we do not have a physical explanation for this slope given that it represents the Lagrangian particle velocity fluctuations and there are distinct differences between the physical properties of our flow and those that have been published. Nevertheless, it is instructive to compare the spectra from the simulations with this seemingly universal slope of $-10/3$ in order to understand how the spectra are modified by clustering. Specifically, when we compare the simulated spectra in figure 9 with the $-10/3$ slope (black dashed line), two humps are identified for low Ar cases ($Ar = 21$ – 1000) while only one hump exists for high Ar cases ($Ar > 1000$). The frequency range of the low-frequency hump decreases as Ar increases while the frequency range of the high-frequency hump increases as Ar increases. Each hump in the spectrum can be interpreted as an accumulation of energy due to frequent particle velocity fluctuations, indicating dominant time scales or frequencies. We hypothesize that these two time scales or frequencies are associated with short- and long-lived clusters. It is likely that the low Ar cases are dominated by long-lived clusters given the larger magnitude of the spectra while the high Ar cases are dominated by short-lived clusters (detailed discussion in § 3.5). Hence, these long-lived clusters behave as a single, larger particle and induce stronger velocity fluctuations (Nicolai *et al.* 1995).

3.4. The effects of Archimedes number on the lifespan and tendency of clustering

To establish a link between the humps observed in the frequency spectra and particle clustering, Voronoï tessellation is used to directly quantify the lifespan and frequency of clusters. In Voronoï tessellation, the domain is decomposed into Voronoï cells in which the centroid of each cell coincides with the centre of a particle. By definition, all points within a Voronoï cell are closer to the centroid of that cell than any other cell. One advantage of the Voronoï tessellation is that an *a priori* length scale is not required, thus reducing the ambiguity in the analysis. Following Uhlmann & Doychev (2014), we define the approximate probability density function (p.d.f.) of quantities associated with randomly arranged particles (Ferenc & Nédá 2007) as

$$f_d(\mathbf{X}) = \frac{((3d+1)/2)^{(3d+1)/2}}{\Gamma((3d+1)/2)} \mathbf{X}^{(3d-1)/2} \exp\left(-\frac{3d+1}{2}\mathbf{X}\right), \quad (3.7)$$

where \mathbf{X} is the random variable representing either the instantaneous Voronoï volume or aspect ratio, $d = 3$ is the dimension of the Voronoï tessellation and Γ is the gamma function. Figure 10(a) shows the distribution of instantaneous Voronoï volumes \mathcal{V} normalized by the ensemble- and time-averaged Voronoï volume $\langle \bar{\mathcal{V}} \rangle$ for different ϕ with $Ar = 21$. Compared with the distribution of randomly arranged particles $f_d(\mathcal{V})$, an increase in ϕ results in a decrease in the width of the p.d.f., indicating a more ordered arrangement. Comparison with different Ar for the same ϕ shows that the effect of Ar (not shown) is negligible, indicating that the distribution of instantaneous $\mathcal{V}/\langle \bar{\mathcal{V}} \rangle$ depends primarily on ϕ . We analysed the geometry of the Voronoï cells by computing the instantaneous aspect ratio of the i th Voronoï cell

$$\mathcal{A}_i = \frac{\max(\ell_{x,i}, \ell_{y,i})}{\ell_{z,i}}, \quad (3.8)$$

where $\ell_{x,i}$, $\ell_{y,i}$ and $\ell_{z,i}$ are the largest separation distances between two vertices in the respective x -, y - and z -directions. Figure 10(b) compares the p.d.f. of \mathcal{A}_i for the cases in this work with the expected p.d.f. from a random arrangement. The probability of observing large \mathcal{A}_i decreases as ϕ increases, indicating a more ordered arrangement due to squeezed/elongated Voronoï cells. This indicates that the particles prefer a vertical arrangement over a horizontal arrangement because of shielding by the upstream particles which reduces the hydrodynamic forces experienced by the downstream particles. However, in the horizontal direction, the shielding effect from the upstream particles is much weaker because the direction of the flow is perpendicular to the arrangement, hence particles are less likely to be aligned horizontally. The vertical-alignment preferences have been observed in all cases simulated which suggests that instantaneous vertical alignment does not induce observable effects on the hindered settling velocity.

To quantify temporal effects, we compute the clustering frequency and lifespan. A cluster is defined as a Voronoï volume satisfying $\mathcal{V}_i < \mathcal{V}_{c,lower}$ and voids as $\mathcal{V}_i > \mathcal{V}_{c,upper}$ where $\mathcal{V}_{c,lower}$ and $\mathcal{V}_{c,upper}$ are the lower and upper bounds defined by the intersection of the simulated p.d.f.s with the randomly arranged p.d.f. given by (3.7). Qualitatively, all simulated cases contain significant numbers of clusters and voids, although more quantitative aspects of clusters concern their lifespan and frequency. More frequent, long-lived clusters can induce appreciable acceleration because clusters can behave as a particle with large inertial effects. To compare the lifespan of clusters across the range of simulated Ar , we utilized the reference time scale $t_{ref} = d_p/w_{ref}$ and computed a

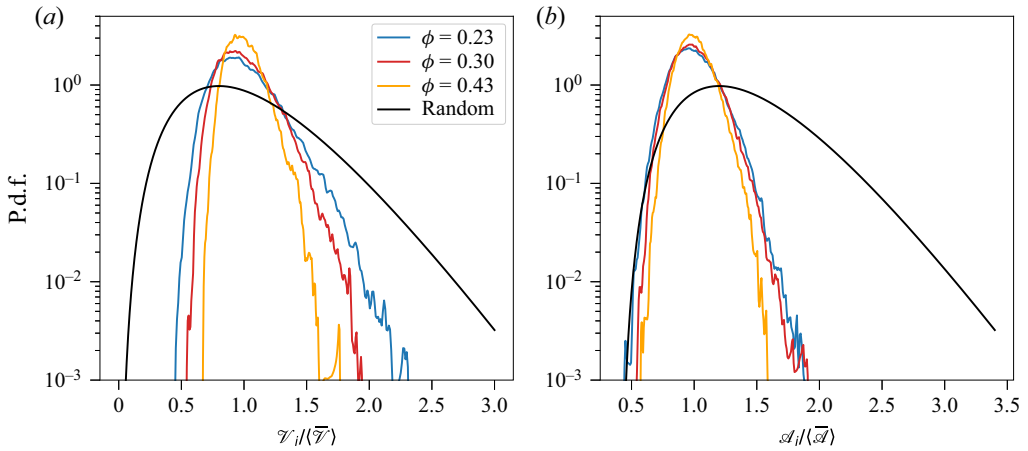


Figure 10. Probability density function of (a) normalized Voronoï volume $\mathcal{V}_i/\langle\mathcal{V}\rangle$ and (b) normalized Voronoï aspect ratio $\mathcal{A}_i/\langle\mathcal{A}\rangle$ as a function of ϕ for $Ar = 21$.

clustering frequency

$$f_{cluster} = \sum_{i=1}^{N_p} \mathbb{1}_{\mathbb{R}^-} \left(\mathbb{1}_{\mathcal{V}_i < \epsilon}(\mathcal{V}_i^{t+1}) - \mathbb{1}_{\mathcal{V}_i < \epsilon}(\mathcal{V}_i^t) \right), \quad (3.9)$$

where $\hat{\mathcal{V}}_i^t$ is the normalized Voronoï volume at time t and $\mathbb{1}_A(X)$ is the indicator function

$$\mathbb{1}_A(X) = \begin{cases} 1 & X \in A, \\ 0 & X \notin A. \end{cases} \quad (3.10)$$

As such, $\mathbb{1}_{\mathcal{V}_i < \epsilon}(\mathcal{V}_i^{t+1}) - \mathbb{1}_{\mathcal{V}_i < \epsilon}(\mathcal{V}_i^t) = 1$ when a particle leaves the cluster, 0 when a particle neither enters nor leaves the cluster and -1 when it enters the cluster. Figure 11(a) shows the normalized clustering frequency $\hat{f}_{cluster} = f_{cluster} t_{ref}$ as a function of Ar . Comparing cases with the same ϕ , as Ar increases, $\hat{f}_{cluster}$ also increases probably because strong velocity fluctuations at higher Ar increase the probability of particles coming into contact with one another (Uhlmann & Doychev 2014), resulting in more clusters. For cases with the same Ar , as ϕ increases, the normalized clustering frequency decreases because more frequent collisions are likely to break apart clusters. Defining the lifespan of clusters as

$$\tau_{clu} = \frac{\sum_{i,t}^{N_p, N_t} \mathbb{1}_{\mathcal{V}_i < \epsilon}(\mathcal{V}_i^t)}{f_{cluster}}, \quad (3.11)$$

figure 11(b) shows the normalized average cluster lifespan $\hat{\tau}_{clu} = \tau_{clu}/t_{ref}$ as a function of Ar and shows that as Ar increases, $\hat{\tau}_{clu}$ significantly decreases. This is probably due to collisions that break apart clusters. Interestingly, taking the inverse of $\hat{\tau}_{clu}$ gives a normalized frequency that falls into the middle of the low-frequency hump for low Ar cases ($Ar = 21$ –1000) and tail of high-frequency hump for high Ar cases in figure 9. This again suggests the humps are due to the particle velocity fluctuations induced by both short- and long-lived clusters. Figure 12 shows the relationship between the normalized Voronoï volumes and the normalized lifespan of clusters. As Ar increases, the slope of dependence decreases drastically, indicating weaker dependence of the lifespan on the

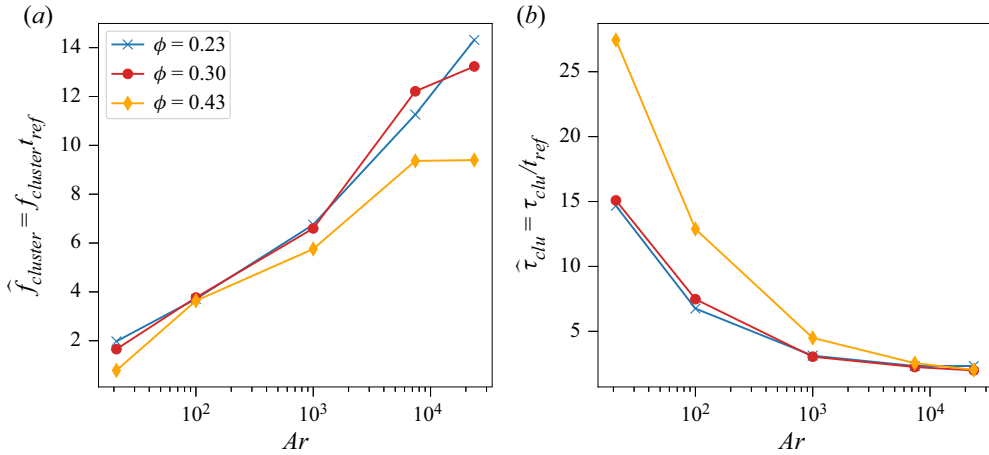


Figure 11. (a) Clustering frequency $f_{cluster}$ and (b) normalized cluster lifespan τ_{clu}/t_{ref} as a function of Ar for different ϕ .

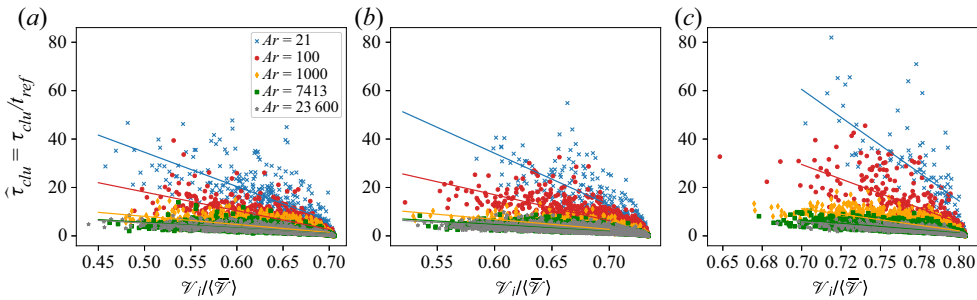


Figure 12. Normalized cluster lifespan τ_{clu}/t_{ref} as a function of normalized Voronoï volume $\mathcal{V}_i/\langle \bar{\mathcal{V}} \rangle$ for different Ar and ϕ : (a) $\phi = 0.23$, (b) $\phi = 0.3$ and (c) $\phi = 0.43$.

Voronoï volumes. As ϕ increases, the dependence of the cluster lifespan on the normalized volumes also increases. Combining the results from the normalized lifespan of clusters and clustering frequency, we show that as Ar increases, the decreased cluster lifespan is accompanied by a significant increase in the clustering frequency which indicates that low Ar is characterized by fewer but longer-lived clusters while high Ar is characterized by more short-lived clusters. Overall, due to a significant number of long-lived clusters in low- Ar particle suspensions, an appreciable increase in the hindered settling velocity is observed, hence resulting in higher k . In contrast, in high- Ar particle suspensions, a large number of short-lived clusters is insufficient to induce appreciable particle acceleration, leading to a lower k .

3.5. Effect of collisions and hydrodynamic forces on clustering

In a concentrated suspension, there are two primary types of interactions, namely fluid–particle interactions induced by hydrodynamic forces and particle–particle interactions induced by collisions. As shown by Esteghamatian *et al.* (2017), the primary role of collisions in concentrated suspensions is to transfer momentum from the axial direction to the transverse direction and induce stronger velocity fluctuations in the transverse directions.

Following Esteghamatian *et al.* (2017) and Nicolai *et al.* (1995), we computed the autocorrelation of the instantaneous particle velocity fluctuation as

$$R_{U_i U_i}(\tau) = \langle U'_{i,n}(t_0) U'_{i,n}(t_0 + \tau) \rangle \quad (3.12)$$

along with the normalized value

$$\widehat{R_{U_i U_i}}(\tau) = \frac{R_{U_i U_i}(\tau)}{\langle U'_{i,n}(t_0) U'_{i,n}(t_0) \rangle}, \quad (3.13)$$

where the fluctuating particle velocity of particle $n = 1, \dots, N_p$ is defined as $U'_{i,n} = U_{i,n} - \langle \bar{U} \rangle_i$, t_0 is a chosen time and $i = x, y$ or z . Here, the overbar is the time-averaging operator defined in (2.5) and the angle bracket $\langle \cdot \rangle$ indicates an ensemble average over all particles. The autocorrelation time scale of the velocity fluctuations is given by

$$\mathcal{T}_i = \lim_{\tau \rightarrow \infty} \int \widehat{R_{U_i U_i}}(\tau) d\tau \quad (3.14)$$

and the self-diffusivity is

$$\mathcal{D}_i = \lim_{\tau \rightarrow \infty} \int R_{U_i U_i}(\tau) d\tau, \quad (3.15)$$

where $i = x, y$ or z .

To quantify the effects of collisions, time- and ensemble-averaged effective collision frequency $\langle f_c \rangle_{eff}$ are computed. A collision between two particles occurs when the separation distance between the particles' centres is less than the particle diameter d_p . As a result, the collision frequency is a monotonically decreasing function of the volume fraction because the likelihood of a collision decreases as the mean separation distance between particles increases. However, this approach leads to overestimation of effective collisions (Ozel *et al.* 2017). Restricting collisions to those with appreciable normal contact velocities is achieved by defining the collision Stokes number

$$St_{imp} = \frac{U_{imp} \rho_p d_p}{9 \rho_f \nu_f}, \quad (3.16)$$

where U_{imp} is the normal component of the relative particle velocities contacting one another. If the number of times a particle n collides with another particle during a simulation time step n_t with $St_{imp} > St_{thresh}$ (where St_{thresh} is the threshold Stokes number, defined below) is given by $\tilde{N}_{c,n}^{n_t}$, then the time- and ensemble-averaged collision frequency is given by

$$\langle \bar{f}_c \rangle_{eff} = \frac{1}{N_p(t_{max} - t_0)} \sum_{l=n_{t,0}}^{n_{t,max}} \sum_{n=1}^{N_p} \tilde{N}_{c,n}^l, \quad (3.17)$$

where $n_{t,0} = t_0 / \Delta t$ and $n_{t,max} = t_{max} / \Delta t$.

The threshold Stokes number is then determined by computing a threshold collision velocity with an empirical function relating the restitution coefficient to the Stokes number. If the vertical velocity of a particle before being subject to lubrication and contact forces

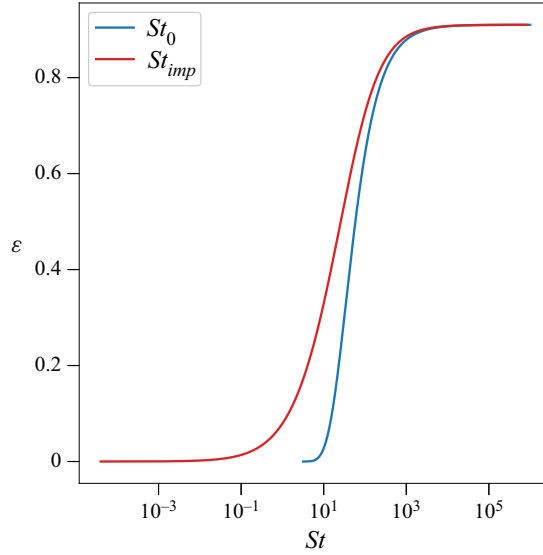


Figure 13. The restitution coefficient ϵ as a function of St_0 and St_{imp} .

is $U_{t,0}$, then the restitution coefficient is given by as

$$\epsilon = \frac{U_r}{U_{t,0}} = \epsilon_{max} \exp\left(-\frac{30}{St_0}\right), \quad (3.18)$$

where U_r is the rebound velocity of a particle after collision and $\epsilon_{max} \approx 0.91$ is the maximum restitution coefficient when $St_0 \rightarrow \infty$, and

$$St_0 = \frac{U_{t,0} d_p \rho_p}{9 \rho_f \nu_f} \quad (3.19)$$

is the Stokes number based on $U_{t,0}$. Figure 13 shows the effect of St_0 on ϵ , demonstrating that a collision is only effective when an appreciable U_r can be achieved for $\epsilon > 0$. We rearranged (3.18) to relate St_{imp} to ϵ by using the dry restitution coefficient $e_{dry} = U_r/U_{imp}$ such that

$$St_{imp} = \frac{30\epsilon}{e_{dry}(\log \epsilon - \log \epsilon_{max})}, \quad (3.20)$$

where U_{imp} is the precollision impact velocity. Figure 13 shows the effect of St_{imp} on ϵ . In this paper, we define $St_{thresh} = 0.22$ as the Stokes number at which $\epsilon = 0.025$, which represents the value of ϵ at which St_{imp} is exceeded by 95% of all values of St_{imp} in figure 13.

To compare the effects of hydrodynamic and collision forces, we computed the ratio of the hydrodynamic fluctuation length scale to the mean free path between collisions $\lambda_{hydro,i}/\lambda_{col,i}$, where

$$\lambda_{hydro,i} = \sqrt{\mathcal{D}_i T_i}, \quad (3.21a)$$

$$\lambda_{col,i} = \sqrt{\mathcal{D}_i / \langle \bar{f}_c \rangle_{eff}}, \quad (3.21b)$$

where $i = x, y$ and z . The mean free path between collisions, $\lambda_{col,i}$, quantifies the average distance the particles travel between collisions, while the hydrodynamic fluctuation

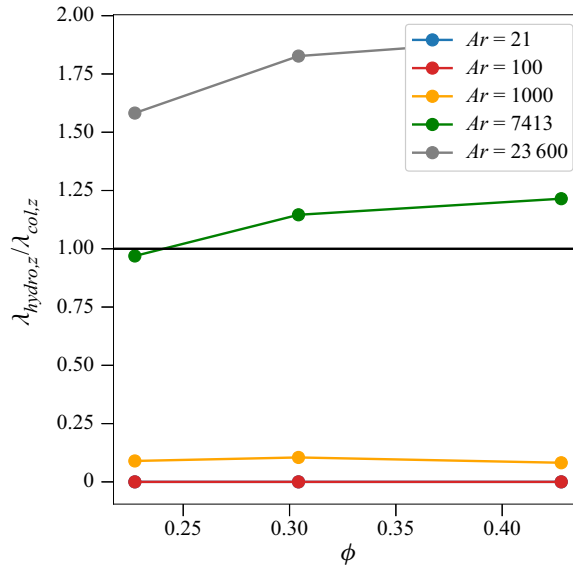


Figure 14. The ratio of vertical hydrodynamic fluctuation length scale $\lambda_{hydro,z}$ to the vertical mean free path between collisions $\lambda_{col,z}$ as a function of volume fraction ϕ for different Ar .

length scale, $\lambda_{hydro,i}$, measures the distance over which the particle velocity fluctuations are still correlated. Figure 14 shows the ratio $\lambda_{hydro,z}/\lambda_{col,z}$ that quantifies the relative effects of hydrodynamic to collision forces. Similar trends are observed for the x - and y -direction (not shown). Since $\lambda_{hydro,z}/\lambda_{col,z} \approx 0$ for $Ar = 21$ and 100 , the mean free path is close to infinitely large, indicating a dominance of hydrodynamic forces without effective particle–particle collisions. Since $0 \leq \lambda_{hydro,z}/\lambda_{col,z} \ll 1$ for $Ar = 1000$, the mean free path is much larger than the hydrodynamic fluctuation length scale, still allowing particles to be influenced by appreciable hydrodynamic forces with few particle–particle collisions. Since $\lambda_{hydro,z}/\lambda_{col,z} \geq 1$ for $Ar = 7413$ and $23\,600$, the mean free path is shorter than the hydrodynamic fluctuation length scale, indicating a dominance of particle collisions, hence particles collide before experiencing appreciable wake interactions induced by hydrodynamic fluctuations. In general, as Ar increases, $\lambda_{hydro,z}/\lambda_{col,z}$ increases significantly indicating $\lambda_{col,z}$ decreases at a rate much faster than the decrease in $\lambda_{hydro,z}$. As a result, the effects of collisions are more significant and dominate over the hydrodynamic forces for high Ar cases, preventing particles from experiencing appreciable wake interactions. Similarly, $\lambda_{hydro,z}/\lambda_{col,z}$ increases slightly with an increase in ϕ , indicating a weak dependence on the volume fraction. As reported by Uhlmann & Doychev (2014), particles cluster and accelerate when they experience appreciable fluctuations induced by wake interactions or the ‘drafting–kissing–tumbling’ effect from interacting particles. In our simulations, particles tend to cluster because of the particle velocity fluctuations and wake interactions at all values of Ar . However, for low Ar cases, clusters are less likely to break up because of insignificant collisions, resulting in long-lived clusters and higher hindered settling or a larger value of k . For high Ar cases, clusters are likely to break up because of strong collisions, leading to short-lived clusters, therefore lower hindered settling and a smaller value of k .

4. Summary and conclusion

We studied the effects of particle properties on the hindered settling velocity in PRS simulations of three-dimensional, triply periodic, monodispersed particle suspensions. The primary parameter of interest is the Archimedes number Ar which is varied by varying the fluid kinematic viscosity ν_f and particle-fluid density ratio s . Analysis of various statistics provided insights into the effects of particle clustering on hindered settling. By plotting the prefactor k obtained from the literature over our simulation results as a function of Ar , we demonstrate that k converges to 0.89 for concentrated suspension as $Ar \rightarrow 0$ and decreases as Ar increases according to an exponential function (3.4), indicating smaller hindered settling for high Ar . We found that the normalized particle velocity fluctuation variance decreases as Ar increases, indicating that particles experience less wake interactions and less ‘drafting-kissing-tumbling’ effects. Frequency spectra demonstrated two humps at low and high frequency for low Ar and one hump at high frequency for high Ar . These humps indicate an accumulation of energy and are likely due to the existence of two types of short- and long-lived particle clusters.

To understand the existence of clustering, we employed Voronoï tessellation to compute the simulated p.d.f. of normalized Voronoï volumes. By comparing the simulated p.d.f. with the p.d.f. of randomly arranged particles, we found that both short- and long-lived clusters exist for all Ar cases with different volume fractions ϕ with the particles favouring vertical alignment, leading to a reduced instantaneous aspect ratio of the normalized Voronoï volumes. The simulated p.d.f.s also suggest that ϕ has stronger effects on the particle arrangement as compared with Ar which more strongly affects particle clustering. By analysing the normalized lifespan and normalized frequency of clusters, we show that the normalized lifespan of clusters decreases with increasing Ar and decreasing ϕ while the normalized frequency of clusters increases with increasing Ar and decreasing ϕ . Both the normalized lifespan and normalized frequency strongly depend on Ar and weakly on ϕ . By analysing the normalized lifespan of clusters as a function of the normalized Voronoï volume, we found that large clusters have longer lifespans for all Ar cases, although the increase in the lifespan is much higher for low Ar cases. Furthermore, the inverses of the cluster lifespans for all Ar cases fall within the dominant humps in the corresponding frequency spectra which indicates energy accumulation is indeed due to particle clustering. This shows that low Ar and high ϕ cases are characterized by less frequent and long-lived clusters while high Ar and low ϕ cases are characterized by more frequent, short-lived clusters.

By quantifying the effects of hydrodynamic forces relative to collision forces with the ratio of the mean free path between collisions $\lambda_{col,z}$ to the hydrodynamic fluctuation length scale $\lambda_{hydro,z}$, we showed that the effects of collisions increase at a rate much faster than the increase in the effects of hydrodynamic fluctuations with increasing Ar , while the effect of ϕ was weak. For $Ar = 21$ and 100 , $\lambda_{hydro,z}/\lambda_{col,z} \approx 0$, indicating that collisions are insignificant and particles can freely experience wake interactions and ‘drafting-kissing-tumbling’ effects, resulting in higher hindered settling and a value of k . When $Ar = 1000$, $0 < \lambda_{hydro,z}/\lambda_{col,z} \ll 1$, the effects of collisions become stronger although particles still experience appreciable wake interactions with less frequent collisions. When $Ar = 7413$ and $23\,600$, $\lambda_{hydro,z}/\lambda_{col,z} > 1$, indicating that the effects of collisions dominate over the hydrodynamic fluctuations. The particles in this regime rarely experience wake interactions because of frequent collisions, resulting in lower hindered settling and a lower value of k .

In application of fluidized-bed reactors for wastewater treatment, flow short circuiting should be minimized to ensure maximum utilization of particle surfaces for optimal

microbial growth and biological degradation. Our results imply that flow short circuiting within fluidized bed reactors is likely to occur when clustering is long-lived. Therefore, our results suggest that operating fluidized-bed reactors in a regime that has short-lived clusters, or with particles having $Ar > 1000$ is likely to reduce flow short circuiting. Though experimental validation of fluidized-bed reactors is needed, previous fluidized bed reactor studies have demonstrated that satisfactory treatment performance is achieved when $Ar = 2000$ – $20\,000$ (Shin *et al.* 2014). We anticipate that the results of this study will inform fluidized-bed reactor design for domestic and industrial wastewater treatment based on Ar , enabling more reliable and energy-efficient operation.

Funding. This work was funded by the California Energy Commission (CEC) under CEC project number EPC-16-017, the US NSF Engineering Center for Reinventing of the Nation's Urban Water Infrastructure (ReNUWIt) under award no. 1028968 and Office of Naval Research Grant N00014-16-1-2256. Simulations were conducted with supercomputer resources under XSEDE Project CTS190063. We thank H. Lee and S. Balachandar from the University of Florida for providing us with their IBM code. We also thank E. Biegert, B. Vowinkel, T. Köllner and E. Meiburg from the University of California, Santa Barbara, for assistance with implementation of the collision models. This document was prepared as a result of work sponsored in part by the California Energy Commission. It does not necessarily represent the views of the Energy Commission, its employees, or the State of California. Neither the Commission, the State of California, nor the Commission's employees, contractors, or subcontractors makes any warranty, express or implied, or assumes any legal liability for the information in this document; nor does any party represent that the use of this information will not infringe upon privately owned rights. This document has not been approved or disapproved by the Commission, nor has the Commission passed upon the accuracy of the information in this document.

Declaration of interests. The authors report no conflict of interest.

Author ORCIDs.

-  Yinuo Yao <https://orcid.org/0000-0001-8328-6072>;
-  Craig S. Criddle <https://orcid.org/0000-0002-2750-8547>;
-  Oliver B. Fringer <https://orcid.org/0000-0003-3176-6925>.

Appendix. Simulation set-up of a fluidized bed

For the simulation of a fluidized bed, three-dimensional simulations are conducted with $N_p = 2000$ particles in a rectangular domain. The particles have an Archimedes number $Ar = 23\,600$. The grid spacing is uniform in the x -, y - and z -directions and the grid resolution is given by $\Delta x = \Delta y = \Delta z = h = d_p/25.6$. The rectangular domain has cross-sectional dimension $L_x = L_y = 10d_p$ and its length is $L_z = 60d_p$ with $256 \times 256 \times 1536$ grid points. The time-step size is $\Delta t = 1.5 \times 10^{-4}$ s, resulting in a maximum advection Courant number of 0.5 for the six cases simulated. The cases are run with periodicity in the x - and y -directions. The pressure is specified at the top boundary as $p = 0$, while at the bottom boundary the inflow velocity is specified as uniform and given by \tilde{U} . The primary parameter of interest is the particle Reynolds number $Re_p = \tilde{U}d_p/\nu_f$, where the average upflow velocity at the inlet, \tilde{U} , is varied to investigate Reynolds number effects. A total of six simulations were conducted with $0.010 \leq \tilde{U} \leq 0.035$, giving $20 \leq Re_p \leq 70$.

REFERENCES

- BATCHELOR, G.K. 1972 Sedimentation in a dilute dispersion of spheres. *J. Fluid Mech.* **52** (2), 245–268.
- BATCHELOR, G.K. 1988 A new theory of the instability of a uniform fluidized bed. *J. Fluid Mech.* **193**, 75–110.
- BATCHELOR, G.K. & WEN, C.-S. 1982 Sedimentation in a dilute polydisperse system of interacting spheres. Part 2. Numerical results. *J. Fluid Mech.* **124**, 495–528.

- BIEGERT, E., VOWINCKEL, B. & MEIBURG, E. 2017 A collision model for grain-resolving simulations of flows over dense, mobile, polydisperse granular sediment beds. *J. Comput. Phys.* **340**, 105–127.
- BORDOLOI, A.D., LAI, C.C.K., CLARK, L., CARRILLO, G.V. & VARIANO, E. 2020 Turbulence statistics in a negatively buoyant multiphase plume. *J. Fluid Mech.* **896**, A19.
- BURTON, F.L., TCHOBANOGLOUS, G., TSUCHIHASHI, R., DAVID TENSEL, H. & METCALF & EDDY, INC. 2013 *Wastewater Engineering: Treatment and Resource Recovery*. McGraw-Hill Education.
- CAPECELATRO, J., DESJARDINS, O. & FOX, R.O. 2015 On fluid–particle dynamics in fully developed cluster-induced turbulence. *J. Fluid Mech.* **780**, 578–635.
- TEN CATE, A., NIEUWSTAD, C.H., DERKSEN, J.J. & VAN DEN AKKER, H.E.A. 2002 Particle imaging velocimetry experiments and Lattice–Boltzmann simulations on a single sphere settling under gravity. *Phys. Fluids* **14** (11), 4012–4025.
- CHONG, Y.S., RATKOWSKY, D.A. & EPSTEIN, N. 1979 Effect of particle shape on hindered settling in creeping flow. *Powder Technol.* **23** (1), 55–66.
- CHOW, E., CLEARY, A.J. & FALGOUT, R.D. 1998 Design of the hypre preconditioner library. In *SIAM Workshop on Object Oriented Methods for Inter-operable Scientific and Engineering Computing*. SIAM.
- DI FELICE, R. 1995 Hydrodynamics of liquid fluidisation. *Chem. Engng Sci.* **50** (8), 1213–1245.
- DI FELICE, R. 1999 The sedimentation velocity of dilute suspensions of nearly monosized spheres. *Intl J. Multiphase Flow* **25** (4), 559–574.
- DI FELICE, R. & PARODI, E. 1996 Wall effects on the sedimentation velocity of suspensions in viscous flow. *AIChE J.* **42** (4), 927–931.
- ESTEGHAMATIAN, A., HAMMOUTI, A., LANCE, M. & WACHS, A. 2017 Particle resolved simulations of liquid/solid and gas/solid fluidized beds. *Phys. Fluids* **29** (3), 033302.
- FALGOUT, R.D. & YANG, U.M. 2002 hypre: a library of high performance preconditioners. In *Computational Science — ICCS 2002* (ed. P.M.A. Sloot, A.G. Hoekstra, C.J.K. Tan & J.J. Dongarra), pp. 632–641. Springer.
- FERENC, J. & NÉDA, Z. 2007 On the size distribution of poisson voronoi cells. *Physica A* **385** (2), 518–526.
- FULLMER, W.D. & HRENYA, C.M. 2017 The clustering instability in rapid granular and gas-solid flows. *Annu. Rev. Fluid Mech.* **49** (1), 485–510.
- GARSDIE, J. & AL-DIBOUNI, M.R. 1977 Velocity-voidage relationships for fluidization and sedimentation in solid-liquid systems. *Ind. Engng Chem. Proc. Des. Dev.* **16** (2), 206–214.
- GONDRET, P., LANCE, M. & PETIT, L. 2002 Bouncing motion of spherical particles in fluids. *Phys. Fluids* **14** (2), 643–652.
- HAMID, A., MOLINA, J.J. & YAMAMOTO, R. 2014 Direct numerical simulations of sedimenting spherical particles at non-zero Reynolds number. *RSC Adv.* **4** (96), 53681–53693.
- JOHNSSON, F., ZIJERVELD, R.C., SCHOUTEN, J.C., VAN DEN BLEEK, C.M. & LECKNER, B. 2000 Characterization of fluidization regimes by time-series analysis of pressure fluctuations. *Intl J. Multiphase Flow* **26** (4), 663–715.
- KEMPE, T. & FRÖHLICH, J. 2012a Collision modelling for the interface-resolved simulation of spherical particles in viscous fluids. *J. Fluid Mech.* **709**, 445–489.
- KEMPE, T. & FRÖHLICH, J. 2012b An improved immersed boundary method with direct forcing for the simulation of particle laden flows. *J. Comput. Phys.* **231** (9), 3663–3684.
- KOWE, R., HUNT, J.C.R., HUNT, A., COUET, B. & BRADBURY, L.J.S. 1988 The effects of bubbles on the volume fluxes and the pressure gradients in unsteady and non-uniform flow of liquids. *Intl J. Multiphase Flow* **14** (5), 587–606.
- LADD, A.J.C. 1989 Hydrodynamic interactions and the viscosity of suspensions of freely moving spheres. *J. Chem. Phys.* **90** (2), 1149–1157.
- LAI, C.C.K. & SOCOLOFSKY, S.A. 2019 The turbulent kinetic energy budget in a bubble plume. *J. Fluid Mech.* **865**, 993–1041.
- LANCE, M. & BATAILLE, J. 1991 Turbulence in the liquid phase of a uniform bubbly air–water flow. *J. Fluid Mech.* **222**, 95–118.
- LI, H., XIA, Y., TUNG, Y. & KWAWK, M. 1991 Micro-visualization of clusters in a fast fluidized bed. *Powder Technol.* **66** (3), 231–235.
- MCCARTY, P.L. 2018 What is the best biological process for nitrogen removal: when and why? *Environ. Sci. Technol.* **52** (7), 3835–3841.
- MORDANT, N. & PINTON, J.-F. 2000 Velocity measurement of a settling sphere. *Eur. Phys. J. B* **18** (2), 343–352.
- NICOLAI, H., HERZHAFT, B., HINCH, E.J., OGER, L. & GUAZZELLI, E. 1995 Particle velocity fluctuations and hydrodynamic self-diffusion of sedimenting non-Brownian spheres. *Phys. Fluids* **7** (1), 12–23.

- VAN OMMEN, J.R., SASIC, S., VAN DER SCHAAF, J., GHEORGHU, S., JOHNSON, F. & COPPENS, M.-O. 2011 Time-series analysis of pressure fluctuations in gas–solid fluidized beds – a review. *Intl J. Multiphase Flow* **37** (5), 403–428.
- OZEL, A., BRÄNDLE DE MOTTA, J.C., ABBAS, M., FEDE, P., MASBERNAT, O., VINCENT, S., ESTIVALEZES, J.-L. & SIMONIN, O. 2017 Particle resolved direct numerical simulation of a liquid–solid fluidized bed: comparison with experimental data. *Intl J. Multiphase Flow* **89**, 228–240.
- RAI, M.M. & MOIN, P. 1991 Direct simulations of turbulent flow using finite-difference schemes. In *27th Aerospace Sciences Meeting, 9th–12th January 1989, Reno, NV, USA. AIAA Paper 1989-369*.
- RENSEN, J., LUTHER, S. & LOHSE, D. 2005 The effect of bubbles on developed turbulence. *J. Fluid Mech.* **538**, 153–187.
- RIBOUX, G., RISSO, F. & LEGENDRE, D. 2010 Experimental characterization of the agitation generated by bubbles rising at high Reynolds number. *J. Fluid Mech.* **643**, 509–539.
- RICHARDSON, J.F. & ZAKI, W.N. 1954 Sedimentation and fluidisation: part I. *Trans. Inst. Chem. Engrs* **32**, 35–53.
- VAN DER SCHAAF, J., SCHOUTEN, J.C., JOHNSON, F. & VAN DEN BLEEK, C.M. 2002 Non-intrusive determination of bubble and slug length scales in fluidized beds by decomposition of the power spectral density of pressure time series. *Intl J. Multiphase Flow* **28** (5), 865–880.
- SCHERSON, Y.D., WOO, S.-G. & CRIDDLE, C.S. 2014 Production of nitrous oxide from anaerobic digester centrate and its use as a co-oxidant of biogas to enhance energy recovery. *Environ. Sci. Technol.* **48** (10), 5612–5619.
- SHIN, C. & BAE, J. 2018 Current status of the pilot-scale anaerobic membrane bioreactor treatments of domestic wastewaters: a critical review. *Bioresour. Technol.* **247**, 1038–1046.
- SHIN, C., KIM, K., MCCARTY, P.L., KIM, J. & BAE, J. 2016 Integrity of hollow-fiber membranes in a pilot-scale anaerobic fluidized membrane bioreactor (AFMBR) after two-years of operation. *Sep. Purif. Technol.* **162**, 101–105.
- SHIN, C., MCCARTY, P.L., KIM, J. & BAE, J. 2014 Pilot-scale temperate-climate treatment of domestic wastewater with a staged anaerobic fluidized membrane bioreactor (SAF-MBR). *Bioresour. Technol.* **159**, 95–103.
- UHLMANN, M. 2005 An immersed boundary method with direct forcing for the simulation of particulate flows. *J. Comput. Phys.* **209** (2), 448–476.
- UHLMANN, M. & DOYCHEV, T. 2014 Sedimentation of a dilute suspension of rigid spheres at intermediate Galileo numbers: the effect of clustering upon the particle motion. *J. Fluid Mech.* **752**, 310–348.
- WILLEN, D.P. & PROSPERETTI, A. 2019 Resolved simulations of sedimenting suspensions of spheres. *Phys. Rev. Fluids* **4** (1), 014304.
- YIN, X. & KOCH, D.L. 2007 Hindered settling velocity and microstructure in suspensions of solid spheres with moderate Reynolds numbers. *Phys. Fluids* **19** (9), 093302.
- ZAIDI, A.A., TSUJI, T. & TANAKA, T. 2015 Hindered settling velocity & structure formation during particle settling by direct numerical simulation. *Procedia Engng* **102**, 1656–1666.
- ZANG, Y., STREET, R.L. & KOSEFF, J.R. 1994 A non-staggered grid, fractional step method for time-dependent incompressible Navier–Stokes equations in curvilinear coordinates. *J. Comput. Phys.* **114** (1), 18–33.